Journal of Southeast University (English Edition) Vol. 40, No. 4, pp. 410 – 416 Dec. 2024 ISSN 1003—7985

# MR damping design of the drive joints of the lunar-based extravehicular spacesuit booster mechanism

Lü Hongzhan Yang Hai Jiang Yu

(College of Mechanical Engineering, Donghua University, Shanghai 201620, China)

**Abstract:** Considering the special walking behavior of astronauts on the lunar surface, to reduce the impact on their bones and improve safety during extravehicular operations and walking, a magnetorheological (MR) damping mechanism of power assisted transmission joint used in a new type spacesuit is proposed. In order to improve the damping performance of the MR damper, the influence of the damper's structural parameters on both the output and dynamic adjustable range of the damping torque is examined. According to the theoretical mechanical model, the output damping torque is calculated, the finite element method is used to conduct numerical tests. At the same time, the structural parameters of the damper are optimized by the response surface methods. The results indicate that the simulated torque aligns with the theoretically designed torque, and the damping characteristics of the optimized structure are effectively improved by the response surface method. Compared with the initial structure, the damping torque is increased by 10.8%, and the dynamic adjustable range is expanded by 52.9%.

**Key words:** extravehicular spacesuit; magnetorheological; flexible transmission; damping characteristics

**DOI:** 10.3969/j.issn.1003 – 7985.2024.04.010

Extravehicular activities are essential for exploring star surfaces, requiring astronauts to carry professional instruments outside their capsules. Given the high-load work astronauts perform, they are prone to musculoskeletal damage[1]. Therefore, it is necessary to develop a spacesuit booster device to address this issue. Various approaches have been explored to develop spacesuit boosters, including the use of artificial muscles or shape-memory alloys as actuating elements[2–3] to compensate for the resistance torque generated by the spacesuit bending. However, the above schemes are unable to reduce the damage to the human body. In aerospace applications, dampers can offer flexible braking and ensure system safety.

**Received** 2024-01-11, **Revised** 2024-05-07.

**Biography:** Lü Hongzhan (1979—), male, doctor, associate professor, lvhz@dhu.edu.cn.

**Foundation item:** The Natural Science Foundation of Shanghai (No. 20ZR1401300).

**Citation:** Lü Hongzhan, Yang Hai, Jiang Yu. MR damping design of the drive joints of the lunar-based extravehicular spacesuit booster mechanism[J]. Journal of Southeast University (English Edition), 2024, 40(4): 410 – 416. DOI: 10.3969/j.issn.1003 – 7985.2024.04.010.

Optimizing damper design can improve the damping characteristics. Saini et al.[4] used a multi-objective particle swarm optimization algorithm to optimize the mass and output damping force of the damper. Li et al.[5] proposed an FNB optimization algorithm that combines the finite element method surrogate model with a novel NM neural network architecture and an alternating stacked beluga whale optimization algorithm to improve the peak torque. Saini et al.[6] used a multi-objective genetic algorithm to optimize braking torque and damper mass. Other studies, including those by Hu et al.[7] have employed multi-objective structural optimization methods to improve the output damping force and dynamic adjustable range. In addition, Wang et al.[8–9] investigated the rotor system variation and optimized the damping characteristics using the finite element method and the Newmark-β method, respectively. The aforementioned schemes have employed various optimization methods to conduct research on damping characteristics.

This article proposes an extravehicular spacesuit power-assist scheme that incorporates magnetorheological (MR) dampers for flexible transmission of spacesuit joints. It enables flexible torque transmission by adjusting the current. Additionally, to maximize the damping characteristics, we apply the response surface method for optimizing the damping torque and its dynamic adjustable range. Ultimately, the efficiency of these optimizations is demonstrated through finite element simulations of pre- and post-optimization results.

## 1 MR Fluid Flexible Joint Transmission Scheme

The flexible joint structure is depicted in Fig. 1. The connection between the motor and the damper determines the maximum radial radius of the damper. Following this, the damper's drive shaft is guided by standard mechanical design principles, while the subsequent optimized structural parameters need to maintain reasonable values between the damper cylinder barrel and the drive shaft.

The theoretical torque of the MR damper is determined to be 1 N · m. However, the actual value of the MR damper torque is smaller than the theoretical estimate, owing to the impact of machining accuracy on the parts. To compensate for this discrepancy, the theoretical torque of the MR damper is set to 1.5 N · m.

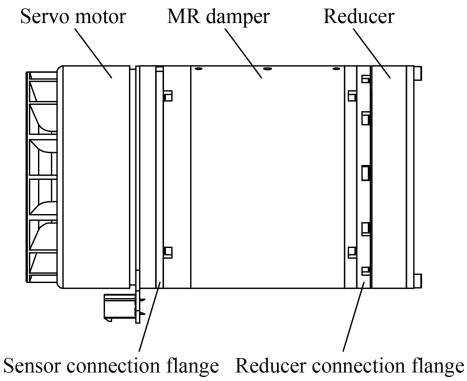


**Fig. 1** Structure of the flexible joint using an MR fluid

## 2 Design of Rotary MR Damper

### 2.1 Selection of initial structural parameters

As shown in Fig. 2, the MR damper mainly consists of the end cap, excitation windings, cylinder barrel, damper rotor, and drive shaft. The end cap, cylinder barrel, and drive shaft are made of No. 20 steel, while the damper rotor is made from electrically pure iron DT4. The material magnetization curve can be obtained from Ref. [10]. The relationship between the magnetic induction intensity and the dynamic shear yield stress of the applied MR fluid MRF450[11] is the following:

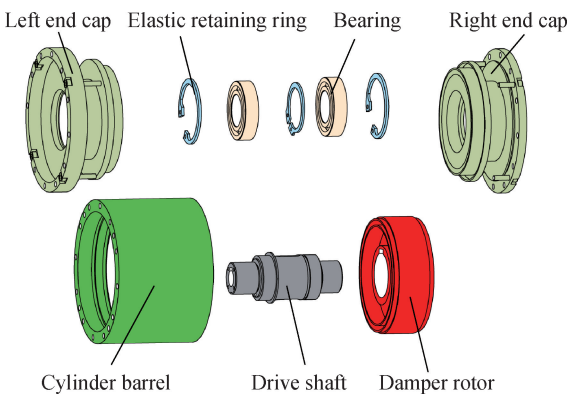


**Fig. 2** Model of the rotary MR damper

$$\tau_y(B) = 25\,827.6B^4 - 45\,068B^3 + 69\,831.3B^2 - 4\,058.4B + 56.14 \quad (1)$$

where $\tau_y(B)$ indicates the dynamic shear yield stress; $B$ represents the magnetic field density.

Owing to the oil film effect[12] of the MR fluid, the gap $h$ of the MR fluid is selected to be 1 mm. The designed structure is shown in Fig. 3, and Table 1 shows the initial structural parameters.

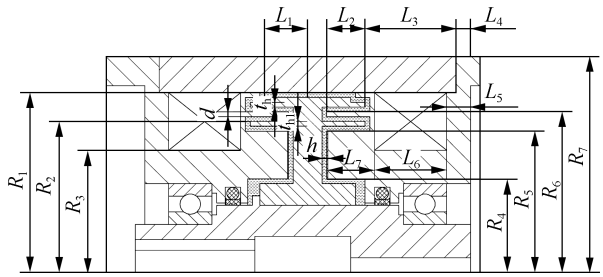


**Fig. 3** Dimensional structure diagram

**Table 1** Initial structural parameters mm

| Fixed-value parameter | Value | Fixed-value parameter | Value |
|---|---|---|---|
| Cylinder bore $R_1$ | 37.5 | Outer fluid length $L_1$ | 9 |
| Damper rotor radius $R_2$ | 31.5 | Effective axial gap $L_2$ | 8 |
| Coil winding radius $R_3$ | 25.5 | Cylinder axial length $L_3$ | 16 |
| End cap inner radius $R_4$ | 20 | Outer thickness of end cap $L_4$ | 3 |
| End cap radial radius $R_5$ | 29.5 | End cap thickness $L_5$ | 5 |
| Contact damping outer radius $R_6$ | 33.5 | Winding axial length $L_6$ | 15 |
| Cylinder outer diameter $R_7$ | 45 | Inner thickness of end cap $L_7$ | 10 |

### 2.2 Design of the magnetic circuit structure

Taking the left end cap as an example (see Fig. 4), the magnetic field lines pass through several components, forming a closed magnetic circuit. These components include the cylinder barrel, the effective damping gap $\delta_1$, the outer-rotor fins' thickness $t_h$, the effective damping gap $\delta_2$, the end cap fins' thickness $d$, the effective damping gap $\delta_3$, the inner-rotor fins' thickness $t_{h1}$, the effective damping gap $\delta_4$, and the end cap.

The magnetomotive force (MMF) $F_m$ in a uniform magnetic circuit can be expressed as

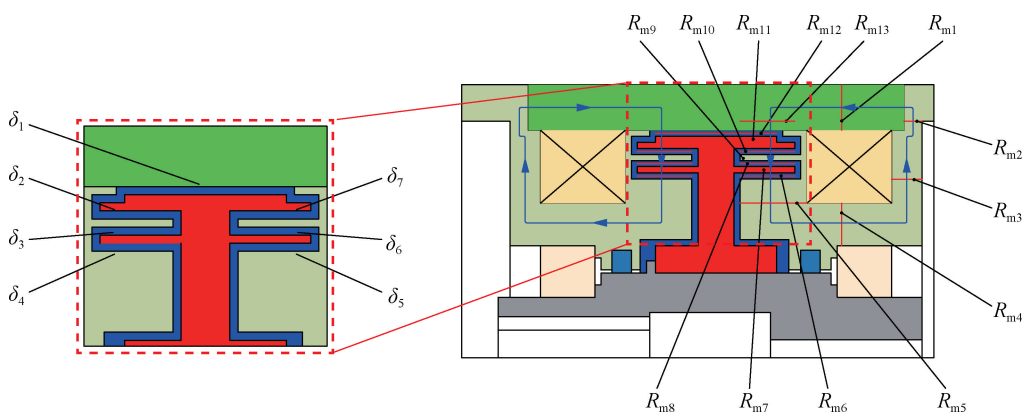


**Fig. 4** Schematic diagram of the magnetic circuit structure

$$F_{\mathrm{m}} = R_{\mathrm{m}}\varphi = NI \tag{2}$$

where $R_{\mathrm{m}}$ is the magnetoresistance; $\varphi$ indicates the magnetic flux; $N$ denotes the winding turns; $I$ represents the current.

The corresponding effective magnetoresistance[13] at different positions is calculated as follows:

$$R_{mi} = \frac{l_i}{\mu_0 \mu_i S_i} \tag{3}$$

where $\mu_0$ is the vacuum permeability; $\mu_i$ is the relative permeability of each effective part of the magnetic circuit; $S_i$ is the area of each effective part; $l_i$ is the effective length of the magnetic circuit.

According to Eq. (3), the total magnetoresistance $R_{\mathrm{m}}$ is calculated to be $8.857\ 2 \times 10^5\ \mathrm{H}^{-1}$, and the total magnetic flux $\varphi$ is found to be 0.628 57 mWb. This causes the total MMF of the magnetic circuit $F_{\mathrm{m}}$ to be 556.739 0 AT. To ensure that the coil current is within the safety margin range, the coil safety current is set to $I = 3$ A, and the number of coil winding turns is rounded to $N = 200$.

### 2.3 Mathematical model of the damping torque

To explicitly describe the rheological properties of MR fluids, the Bingham model[14] was adopted as the foundation for deriving the mathematical model of the damping torque.

$$\tau = \tau_{\mathrm{y}}(B) + \eta\dot{\gamma} = \tau_{\mathrm{y}}(B) + \eta r\frac{\omega}{g} \tag{4}$$

where $\tau$ is the shear stress of the MR fluid; $\eta$ is the zero-field viscosity; $\dot{\gamma}$ is the shear strain rate; $r$ is the working radius of the damping gap; $\omega$ is the angular velocity.

The total output damping torque $T$[15] generated by the MR fluid in response to a magnetic field at radius $r$ is expressed as follows:

$$T = \tau_{\mathrm{y}}(B)2\pi r^2 L + \eta r\frac{\omega}{g}2\pi r^2 L + T_{\mathrm{m}} = T_B + T_\eta + T_{\mathrm{m}} \tag{5}$$

where $L$ is the axial length of the effective working gap of the MR fluid.

The total output torque of the damper consists of three parts. The first part is the hysteresis torque $T_B$ generated by the MR fluid in response to the magnetic field. The second part is the viscous torque $T_\eta$ generated by the viscosity characteristics of the MR fluid itself, while the third part is the total friction torque $T_{\mathrm{m}}$ generated between the sealing element and the rotating shaft.

The kinematic friction $F_{\mathrm{s}}$[16] generated by the sealing element is the following:

$$F_{\mathrm{s}} = 2\pi f D l_0 p_{\mathrm{cm}} \tag{6}$$

where $f$ is the friction coefficient; $D$ is the diameter of the friction surface of the sealing element; $l_0$ is the width of the contact surface; $p_{\mathrm{cm}}$ is the average contact pressure of the friction surface[17]. Considering the above data, the friction torque generated by a single sealing element can be obtained as $T_{\mathrm{one}} = F_{\mathrm{s}}D/2 = 0.27\ \mathrm{N \cdot m}$.

The dynamic adjustable range $K$ indicates the ratio of hysteresis torque $T_B$ and viscous torque $T_\eta$[18]:

$$K = \frac{T_B}{T_\eta} \tag{7}$$

## 3 Simulation Analysis of Magnetic Current Coupling

### 3.1 Simulation results

Through magnetic field simulations, we obtained the distribution of the magnetic field density, as shown in Fig. 5, and extracted the magnetic field density data at each damping gap (see Table 2).

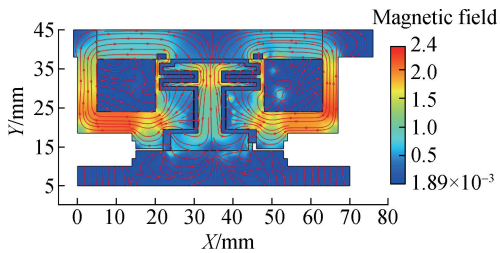


**Fig. 5** Distribution of the magnetic field density

**Table 2** Average magnetic induction for each damping gap

T

| $\delta_1$ | $\delta_2$ | $\delta_3$ | $\delta_4$ | $\delta_5$ | $\delta_6$ | $\delta_7$ |
|---|---|---|---|---|---|---|
| 0.391 5 | 0.064 5 | 0.093 0 | 0.299 0 | 0.309 3 | 0.096 9 | 0.070 0 |

Owing to the opposing directions of the magnetic field, the magnetic field density concentrates in the damping gaps, with its values listed in Table 2. The magnetic field density is maximum at the damping gap $\delta_1$, while it is approximately 0.3 T at damping gaps $\delta_4$ and $\delta_5$, and under the effect of magnetoresistance, it is the smallest at the damping gaps $\delta_2$, $\delta_3$, $\delta_6$, and $\delta_7$.

Substituting the magnetic induction from Table 2 into Eq. (1) and then incorporating the dynamic shear yield stress into Eq. (5), we can calculate the total damping torque $T_{\mathrm{total}} = 2.389\ \mathrm{N \cdot m}$.

As shown in Fig. 6, the simulation result shows that the total simulated torque $T$ is $2.275\ \mathrm{N \cdot m}$. It can be seen that the simulation and theoretical calculations meet the expected set damping torque.

When the drive shaft rotates, the effective damping gap $\delta_1$ experiences the largest centrifugal force, resulting in the pressure value at this gap $\delta_1$. Conversely, the pressure values at the damping gaps $\delta_4$ and $\delta_5$, which are located internally, are the smallest. The pressure values are illustrated in Fig. 7.

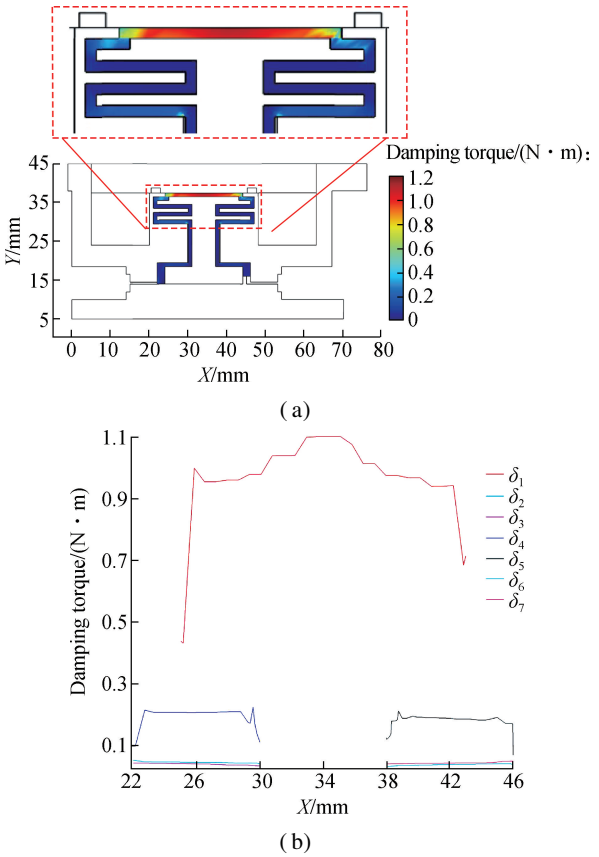


**Fig. 6** Damping torque in simulations. (a) Cloud image distribution; (b) Damping torque of each damping gap

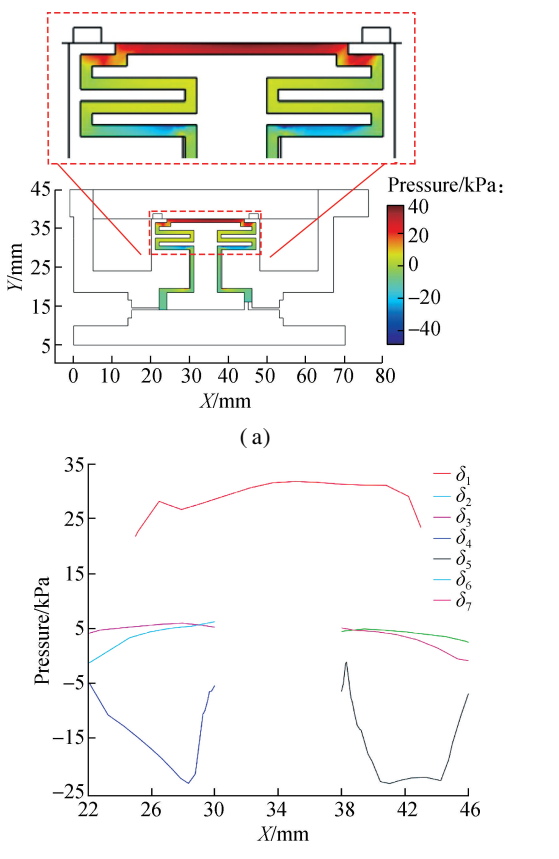


**Fig. 7** Pressure distribution of the MR fluid. (a) Cloud image distribution; (b) Pressure of each damping gap

### 3.2 Single-factor impact analysis

The thickness of the outer fins of the rotor $t_h$ varies from 1.0 to 5.0 mm. According to Eq. (5), the damping torque generated by the damper is affected by the magnetic field intensity and the damping radius. The magnetic field intensity at $\delta_2$, $\delta_3$, $\delta_6$, and $\delta_7$ are small (see Fig. 8(a)), with the magnetic field intensity at $\delta_1$ being the largest. The magnetic field intensity at $\delta_1$ reaches its maximum at $t_h = 3$ mm, which corresponds to the peak of the damping torque in Fig. 8(b).

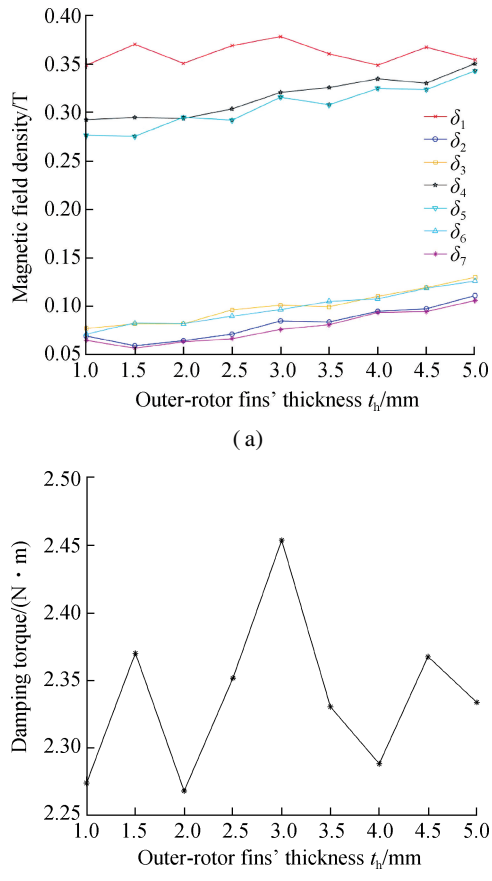


**Fig. 8** Thickness of the outer-rotor fins. (a) Magnetic field intensity; (b) Damping torque

The fin thickness $d$ of the end cap ranges from 1.0 to 4.0 mm. As $d$ increases, the magnetic field intensity at $\delta_2$ to $\delta_7$ varies slightly, and when the magnetic field intensity at $\delta_1$ reaches a maximum value at $d = 2$ mm, the corresponding damping torque also reaches a peak value (see Fig. 9).

The thickness of the inner fins of the rotor $t_{h1}$ varies from 1.0 to 5.0 mm. As shown in Fig. 10, changes in the $t_{h1}$ weakly affect the magnetic induction intensity at $\delta_1$, while the magnetic field intensity at $\delta_4$ and $\delta_5$ increases significantly. Consequently, the total output damping torque reaches its maximum at $t_{h1} = 4.5$ mm.

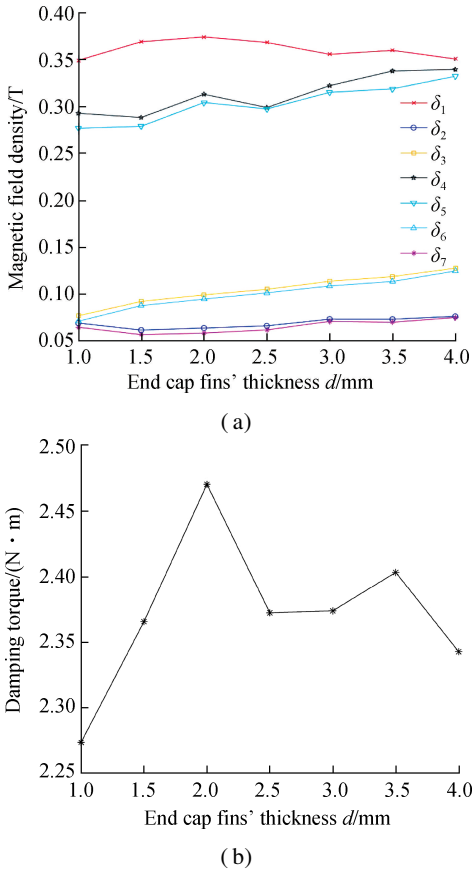


**Fig. 9** Thickness of the end cap. (a) Magnetic field intensity; (b) Damping torque

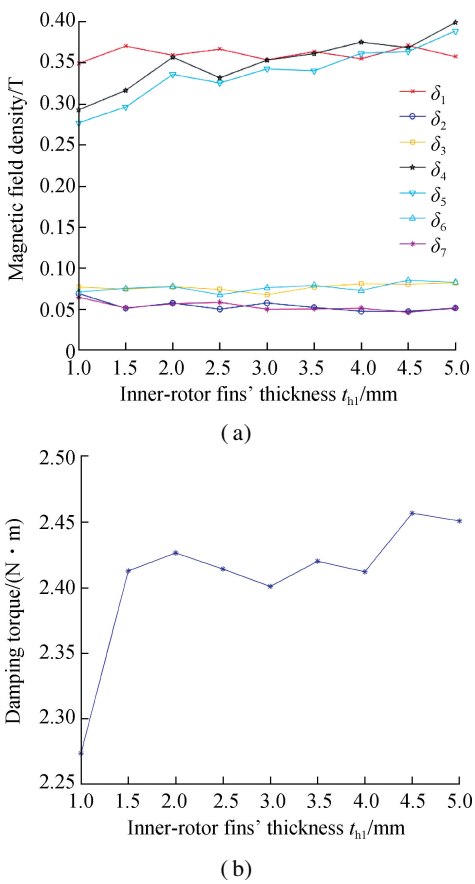


**Fig. 10** Thickness of the inner-rotor fins. (a) Magnetic field intensity; (b) Damping torque

## 4 Optimization Based on Response Surface Methodology

### 4.1 Response surface test design

To enhance damping characteristics without increasing the damper's volume, we selected the structural parameters in the radial direction as the design variables. The values are listed in Table 3.

**Table 3** Upper and lower limits of design variables

| Design variable | Lower limit | Upper limit |
|---|---|---|
| Thickness of outer-rotor fins $t_h$ | 1 | 5 |
| Thickness of end cap fins $d$ | 1 | 4 |
| Thickness of inner-rotor fins $t_{h1}$ | 1 | 5 |

The hysteresis torque $T_B$ and viscous torque $T_\eta$ can be obtained through simulations, and the dynamic adjustable range can be calculated by combining Eq. (7). The results are listed in Table 4.

**Table 4** Design and results of response surface tests

| Test number | $t_h$ | $d$ | $t_{h1}$ | Damping torque $T$/(N · m) | Dynamic adjustable range $K$ |
|---|---|---|---|---|---|
| 1 | 1 | 1 | 3 | 2.555 21 | 5.298 18 |
| 2 | 1 | 4 | 3 | 2.469 04 | 5.611 61 |
| 3 | 5 | 1 | 3 | 2.580 13 | 6.739 01 |
| 4 | 5 | 4 | 3 | 2.099 29 | 5.662 48 |
| 5 | 3 | 1 | 1 | 2.466 99 | 5.506 81 |
| 6 | 3 | 4 | 1 | 2.387 24 | 5.847 73 |
| 7 | 3 | 1 | 5 | 2.559 84 | 6.128 56 |
| 8 | 3 | 4 | 5 | 1.955 08 | 4.650 8 |
| 9 | 1 | 2.5 | 1 | 2.470 64 | 5.183 55 |
| 10 | 5 | 2.5 | 1 | 2.385 88 | 6.223 28 |
| 11 | 1 | 2.5 | 5 | 2.373 83 | 5.219 48 |
| 12 | 5 | 2.5 | 5 | 1.992 02 | 5.407 94 |
| 13 | 3 | 2.5 | 3 | 2.426 24 | 5.853 77 |

### 4.2 Response surface model

The regression equation for the response surface methodology (RSM) can be described as follows[19]:

$$y = \hat{y}(x_1, x_2, \ldots, x_n) + \varepsilon \tag{8}$$

where $y$ is the response target; $x_1, x_2, \ldots, x_n$ are design variables; $\varepsilon$ is the error between the actual response value and the approximate one. In this paper it can be described by a quadratic model.

$$y = \beta_0 + \sum_{i=1}^{k} \beta_i x_i + \sum_{i=1}^{k} \beta_{ii} x_i^2 + \sum_{i,j\neq i}^{k} \beta_{ij} x_i x_j + \varepsilon \tag{9}$$

where $\beta_0$, $\beta_i$, $\beta_{ii}$, and $\beta_{ij}$ are the regression coefficients to be estimated.

Utilizing the data in Table 4 and Eq. (9), we can derive a regression equation regarding damping torque and dynamic adjustment range.

$$T = 0.087\ 207 t_h + 0.125\ 628 d + 0.113\ 202 t_{h1} -$$

$$0.032\,889t_h d - 0.018\,566t_h t_{h1} - 0.043\,752dt_{h1} + 2.189\,79 \quad (10)$$

$$K = -0.006\,359t_h^2 - 0.000\,232d^2 - 0.079\,945t_{h1}^2 - 0.115\,83t_h d - 0.053\,2t_h t_{h1} - 0.151\,556dt_{h1} + 0.657\,332t_h + 0.644\,988d + 0.933\,51t_{h1} + 2.731\,19 \quad (11)$$

From the experimental results, the determination coefficient for the damping torque is $R^2 = 0.92$, and the determination coefficient of the dynamic adjustable range is $R^2 = 0.99$, indicating that the model has a high degree of fitting and can be used for reasonable predictions.

### 4.3 Optimization results

Through the regression equation of the response target, the optimal structural parameters to achieve the maximum output damping torque and dynamic adjustable range have been identified as $t_h = 5$ mm, $d = 1$ mm, and $t_{h1} = 3$ mm, which correspond to the output damping torque and dynamic adjustable range of $T_p = 2.52$ N · m and $K_p = 6.753$ respectively. The detailed data are listed in Table 5.

**Table 5** Structural parameters and damping characteristics before and after optimization

| Parameters | $t_h$/mm | $d$/mm | $t_{h1}$/mm | $T$/(N · m) | $K$ |
|---|---|---|---|---|---|
| Initial parameters | 1 | 1 | 1 | 2.275 | 4.416 |
| Optimization parameters | 5 | 1 | 3 | 2.520 | 6.753 |

Compared with the initial structure, the optimized damping torque is increased by 10.8%, and the dynamic adjustable range is increased by 52.9%. These results show that the adopted optimization method effectively improves the output damping torque and dynamic adjustable range of the damper.

## 5 Conclusions

1) We designed a variable stiffness actuation scheme aimed at providing flexible damping torque for astronauts' space motion, which effectively mitigates the impact on astronauts.

2) Under the initial structural conditions, both the theoretical calculation and simulation solutions result in damping torques that meet the preset target, demonstrating the rationality of the initial structural design.

3) By employing the response surface method, two important parameters, namely damping torque and dynamic adjustable range, are optimized. Compared with the initial structure, the optimized damping torque increased by 10.8% and the dynamic adjustable range increased by 52.9%.

## References


[1] Holschuh B, Newman D. Extravehicular activity (EVA) [M]//*Handbook of Bioastronautics*. Cham: Springer International Publishing, 2021: 83 – 90. DOI: 10.1007/978-3-319-12191-8_18.

[2] Villoslada Á, Rivera C, Escudero N, et al. Hand exomuscular system for assisting astronauts during extravehicular activities[J]. *Soft Robotics*, 2019, **6**(1): 21 – 37. DOI: 10.1089/soro.2018.0020.

[3] Zhou M L, Hou W G, Xu S H. Design and analysis of power assist elbow for EVA spacesuit[J]. *Applied Mechanics and Materials*, 2014, **577**: 395 – 400. DOI: 10.4028/www.scientific.net/amm.577.395.

[4] Saini R S T, Kumar H, Chandramohan S. Optimal design of flow mode semi-active prosthetic knee dampers[J]. *Scientia Iranica*, 2022, **29**(6): 3049 – 3062. DOI: 10.24200/sci.2022.58926.5971.

[5] Li J H, Zhou W, Deng X X, et al. Magnetorheological dampers optimization based on surrogate model and experimental verification[J]. *International Journal of Mechanical Sciences*, 2024, **270**: 109093. DOI: 10.1016/j.ijmecsci.2024.109093.

[6] Saini R S T, Chandramohan S, Sujatha S, et al. Design of bypass rotary vane magnetorheological damper for prosthetic knee application[J]. *Journal of Intelligent Material Systems and Structures*, 2021, **32**(9): 931 – 942. DOI: 10.1177/1045389x20942577.

[7] Hu G L, Ying S C, Qi H N, et al. Design, analysis and optimization of a hybrid fluid flow magnetorheological damper based on multiphysics coupling model[J]. *Mechanical Systems and Signal Processing*, 2023, **205**: 110877. DOI: 10.1016/j.ymssp.2023.110877.

[8] Wang J, Liu Y F, Qin Z Y, et al. Dynamic performance of a novel integral magnetorheological damper-rotor system[J]. *Mechanical Systems and Signal Processing*, 2022, **172**: 109004. DOI: 10.1016/j.ymssp.2022.109004.

[9] Wang J, Zhang X N, Liu Y F, et al. Dynamic analysis of magnetorheological damper incorporating elastic ring in coupled multi-physical fields[J]. *Mechanical Systems and Signal Processing*, 2024, **208**: 111040. DOI: 10.1016/j.ymssp.2023.111040.

[10] Technical Qualification Appraisal and Evaluation Committee of Non-destructive Testing Personnel in Ordnance Industry. *Quick reference manual of magnetic characteristic curve of common steels*[M]. Beijing: Machinery Industry Press, 2003: 17. (in Chinese)

[11] Wei L K, Lü H Z, Yang K H, et al. A comprehensive study on the optimal design of magnetorheological dampers for improved damping capacity and dynamical adjustability[J]. *Actuators*, 2021, **10**(3): 64. DOI: 10.3390/act10030064.

[12] Zuo Q, Zhou F, Zheng H, et al. Development and performance evaluation of rotary magnetorheological damper with T-shape rotor for seat suspension[J]. *Journal of the Brazilian Society of Mechanical Sciences and Engineering*, 2021, **43**(12): 563. DOI: 10.1007/s40430-021-03298-6.

[13] Xu F H, Xu Z D. Magnetic circuit analysis on multi-coil magnetorheological damper[J]. *Journal of Southeast University (Natural Science Edition)*, 2016, **46**(1): 100 – 104. DOI: 10.3969/j.issn.1001-0505.2016.01.017. (in Chinese)

[14] Xie W X, Liu J P, Li Z, et al. Influence of recycled

powders on yield stress of cement paste with superplasticizer and its mechanism[J]. *Journal of Southeast University* (*Natural Science Edition*), 2023, **53**(4): 567 – 574. DOI: 10.3969/j.issn.1001-0505.2023.04.001. (in Chinese)

[15] Dai J Q, Song A G, Wang A M. Novel magnetorheological fluid damper for passive force/torque feedback[J]. *Journal of Southeast University* (*English Edition*), 2007, **23**(1): 70 – 74. DOI: 10.3969/j.issn.1003-7985.2007.01.015.

[16] Gu Y Q. *Fluid dynamic seals*[M]. Beijing: Sinopec Press, 1990: 31. (in Chinese)

[17] Li J Y. *Experimental study on the characteristics of gas-protected jet and rock-breaking*[D]. Qingdao: China University of Petroleum, 2008. (in Chinese)

[18] Huang J, Zhang J Q, Yang Y, et al. Analysis and design of a cylindrical magneto-rheological fluid brake[J]. *Journal of Materials Processing Technology*, 2002, **129**(1/2/3): 559 – 562. DOI: 10.1016/S0924-0136(02)00634-9.

[19] Zhang C J, Chen Z H, Mei Q X, et al. Application of particle swarm optimization combined with response surface methodology to transverse flux permanent magnet motor optimization[J]. *IEEE Transactions on Magnetics*, 2017, **53**(12): 8113107. DOI: 10.1109/TMAG.2017.2749565.

# 月基舱外航天服助力机构传动关节磁流变阻尼设计

吕宏展 杨 海 江 宇

(东华大学机械工程学院, 上海 201620)

**摘要**:针对航天员在月表工作时的特殊行走行为,为了减少航天员舱外作业及行走时对身体骨骼造成的冲击,提高航天员月基舱外作业的安全性,提出了一种应用于新型航天服的助力装置传动关节磁流变阻尼机构.为了提高磁流变阻尼器的阻尼性能,研究阻尼器结构参数对磁流场中阻尼力矩的输出和动态调节范围的影响,根据理论力学模型,计算输出阻尼力矩,并采用有限元方法进行数值试验;同时,采用响应面法,对阻尼器结构参数进行优化.结果表明:仿真力矩达到了设计的理论力矩,通过响应面优化后的结构,其阻尼特性得到有效提升;与初始结构相比,阻尼力矩提高了10.8%,动态调节范围增大了52.9%.

**关键词**:舱外航天服;磁流变;柔性传动;阻尼特性

**中图分类号**:V444.3